Atmospheric
Measurement
Techniques
Discussions

The transport of bioaerosols observed by wideband integrated bioaerosol sensor and coherent Doppler lidar

Dawei Tang[1], Tianwen Wei[1], Jinlong Yuan[1], Haiyun Xia[1,2,3,*], Xiankang Dou[1,4]

[1]CAS Key Laboratory of Geospace Environment, School of Earth and Space Science, USTC, Hefei 230026, China

[2]Hefei National Laboratory for Physical Sciences at the Microscale, Hefei 230026, China

[3]CAS Center for Excellence in Comparative Planetology, Hefei 230026, China

[4]School of Electronic Information, Wuhan University, Wuhan 430072, China

Correspondence to: Haiyun Xia (hsia@ustc.edu.cn)

Abstract. Bioaerosols are usually defined as aerosols derived from biological systems such as bacteria, fungi, and viruses. They play an important role in atmospheric physical and chemical processes including ice nucleation and cloud condensation. As such, their dispersion affects not only public health but regional climate as well. Lidar is an effective technique for aerosol detection and pollution monitoring. It is also used to profile the vertical distribution of wind vectors. In this paper, a coherent Doppler wind lidar (CDWL) was deployed for wind and aerosol detection in Hefei, China, from 11 to 20 March in 2020. A wideband integrated bioaerosol sensor (WIBS) was deployed to monitor variations in local fluorescent bioaerosol levels. During observation, three aerosol transport events were captured. The WIBS data show that during these transport events, several types of fluorescent aerosol particles exhibit abnormal increases in either their concentration, number fractions to total particles, or number fractions to whole fluorescent aerosols. These increases are attributed to transported external fluorescent bioaerosols instead of local bioaerosols. Based on the Hybrid Single Particle Lagrangian Integrated Trajectory (HYSPLIT) backward trajectory model and the characteristics of external aerosols in WIBS, their possible sources, transport paths, and components are discussed. This work proves the influence of external aerosol transport on local high particulate matter (PM) pollution and fluorescent aerosol particle composition. The combination of WIBS and CDWL expands the aerosol monitoring parameters and proves to be a potential method for the real-time monitoring of fluorescent biological aerosol transport events. It contributes to the further understanding of bioaerosol transport.

Atmospheric
Measurement
Techniques

Discussions

1.   Introduction

Aerosols are suspensions of fine solid particles or liquid droplets in the atmosphere. Biological aerosols

30   or bioaerosols are atmospheric aerosols derived from biological sources in a broad sense. In a narrow

sense, bioaerosols refer to primary biological aerosol particles (PBAP), which means biological material

directly emitted to the atmosphere rather than being formed through gas-to-particle conversion. The latter

are called Biogenic Secondary Organic Aerosols and are beyond the scope of this paper. Bioaerosols

show great diversity in species, including bacteria, fungi, viruses, pollen, algae, and their fragments.

35   Their sizes consequently range from a few nanometers to hundreds of microns. Due to their

hygroscopicity (Petters and Kreidenweis, 2007), bioaerosols show higher efficiency in acting as ice

nuclei (IN) and cloud condensation nuclei (CCN) compared with non-organic aerosols. Thus, they have

an important impact on regional climate by participating in atmospheric physical and chemical processes,

including cloud formation and precipitation. Bioaerosols are also associated with health problems

40   including infectious, toxic, and hypersensitivity diseases. Some kinds of bioaerosols have the potential

to be used for bioterrorism. Therefore, in recent years bioaerosols have been drawing increasing amounts

of attention.

Due to the diffusion caused by atmospheric turbulence below the planetary boundary layer (PBL), surface

aerosol particles are mainly dispersed in the PBL. This dispersion continues until they are removed from

45   the atmosphere by the dry or wet deposition process. However, under specific conditions, a fraction of

aerosol particles may be entrained above the PBL and enter the free troposphere. Once there, aerosol

particles are no longer affected by the height of the PBL or its daily behavior and can perform long-range

transport under the action of wind or sandstorms until re-entry to the PBL via transport. Bioaerosols have

developed some survival mechanisms including pigment deposition, sporulation, and attaching

50   themselves to particles, which allows them to survive in dry and intense solar radiation environments at

high altitudes during long-range transport.

There is increasing evidence to show the long-range transport capability and pathways of bioaerosols. In

Asia, bioaerosols are frequently observed being transported along with dust during Asian dust events.

These affect the concentrations and structures of airborne biological communities in the surrounding area.

55   In Japan, Asian dust events affect airborne bacteria communities in the air near the surface and free

troposphere (Hua et al., 2007; Maki et al., 2014, 2015). An increased level of fungal spores was found in

Hualien, Taiwan during sandstorms originating from Asian deserts (Ho et al., 2005; Wu et al., 2004). In Korea, Asian dust events impact airborne fungal concentrations and communities (Jeon et al., 2011, 2013). DAPI staining and DNA sequencing results show an increased level of airborne bacteria

60   concentrations and diversity in Northern China during Asian dust events (Tang et al., 2017). However, these studies are based on aerosol sampling technologies and offline analyses such as microscopy analysis and DNA sequencing. These offline analysis methods limit the temporal resolution during monitoring and the detection time for the external aerosol transport event. These sampling and offline analysis methods provide a typical time resolution ranging from a few hours to a few days, which may

65   not provide the ability to distinguish the bioaerosol process over a short time scale from the slower bioaerosol long-term variation trend.

To overcome these challenges, several online measurement instruments using light-induced fluorescence (LIF) technologies have been developed(Fennelly et al., 2017) based on the autofluorescent properties of bioaerosol. These instruments monitor fluorescent aerosol particles (FAPs) as a proxy for bioaerosol

70   particles. The wideband integrated bioaerosol sensor (WIBS, Droplet Measurement Technologies, Inc.) detects the biological fluorescent component of aerosol particles, such as Tryptophan, Riboflavin, or NADH during measurement. It can provide time-dependent characteristics for different types of FAPs and non-FAPs. However, it should be noted that there are non-biological fluorescent components on aerosol particles, such as polycyclic aromatic hydrocarbons (PAHs), humic acids, and fulvic acids. These

75   may act as interference during WIBS measurements. In recent years, WIBS has been widely used under different conditions such as at high altitudes (Crawford et al., 2016; Yue et al., 2019), forests, rainforests (Gabey et al., 2011), seashore (Daly et al., 2019), rural areas (Healy et al., 2014), urban areas (Cheng et al., 2020; Ma et al., 2019; Yu et al., 2016; Yue et al., 2016) and in airborne observations (Perring et al., 2015; Ziemba et al., 2016). These measurement campaigns prove its effectiveness and consistency with

80   other offline detection results (Feeney et al., 2018; Fernández-Rodríguez et al., 2018).

Direct real-time observations of aerosol transport help us to understand this process comprehensively. As an active remote sensing detection tool, lidar can provide long-term continuous high spatial and temporal resolution monitoring of aerosol and wind vector vertical profiles. In recent years, ground-based and satellite-borne lidar combined with other observation data on the ground, such as meteorology, O_3,

85   and particulate matter (PM) concentration data, have been widely used to observe and study haze or pollution episodes caused by aerosol transboundary transport (Fang et al., 2021; Huang et al., 2021; Qin

3

et al., 2016; Wang et al., 2019; Yang et al., 2021a, 2021b). However, the above studies were limited to using local PM concentration data to characterize the monitored aerosols, while the variations of different types of aerosols are not characterized.

90 In this paper, a coherent Doppler wind lidar (CDWL) system is used to observe the vertical profile of atmospheric aerosols and wind over Hefei, China. A WIBS was used to monitor the concentration and time variation of various types of local fluorescent bioaerosol particles from 11 to 20 March 2020. During observation, three aerosol transport events were captured and abnormal changes in some types of fluorescent aerosols during these events were shown in WIBS data. After an analysis combining local

95 meteorological data and Hybrid Single Particle Lagrangian Integrated Trajectory (HYSPLIT) backward trajectory model, these abnormal changes in WIBS data are attributed to transport from external fluorescent bioaerosols. The possible types and origins of external aerosols are discussed.

In Sect. 2 the instrument parameters, experimental sites, data used, and processing method are introduced. The observation results during each event are discussed in Sect. 3. The conclusions are given in Sect. 4.

100 ## 2. Data and Method

2.1. Ground-based lidar measurements

In this study, a CDWL system is utilized. The CDWL emits pulsed laser at a repetition rate of 10 kHz with 100 μJ of pulse energy and operates at an eye-safe wavelength of 1.5 μm. Detailed information about the system and its applications can be seen in previous work (Jia et al., 2019; Wei et al., 2019,

105 2020; Yuan et al., 2020).

During observation, the lidar system is located on grassland near the School of Earth and Space Science building on the campus of the University of Science and Technology of China in Hefei, Anhui Province, China. It is set to operate in the velocity-azimuth display (VAD) scanning mode with a fixed elevation angle of 60°. The carrier-to-noise ratio (CNR), Doppler spectral width, and radial wind speed are saved

110 as Level-1 data. Wind vector profiles are then retrieved by the filtered sine wave fitting (FSWF) method (Banakh et al., 2010). A positive vertical speed value in Lidar data indicates a downward direction and otherwise the opposite. The Doppler spectral width is an indicator of turbulence. In addition, it can also be broadened during rainfall events (Wei et al., 2021).

The attenuated backscatter coefficient (β') is derived by a semi-qualitative method (Pentikäinen et al.,

115   2020) from CNR and calculated by

$$\beta'(R) = C \frac{CNR(R)}{T_f(R)} \; , \tag{1}$$

Where C is a calibration factor related to the pulse energy and optical attenuation (O'Connor et al., 2004).

The focus function $T_f(R)$ is a telescope function and is derived by low elevation scans over a

homogeneous surface (Yang et al., 2020). This method has been applied and its effectiveness proved in

120   Hong Kong and Iceland observation campaigns (Huang et al., 2021; Yang et al., 2020). The lower

threshold of CNR is set to -35 dB for low uncertainty in β' retrieval.

2.2. PM data and meteorological data

$PM_{2.5}$ and PM_{10} represent particulate matter with aerodynamic diameters less than or equal to 2.5 μm and

10 μm respectively. At present, many cities in China have established stations with $PM_{2.5}$ and PM_{10}

125   monitoring capabilities, which constitute a part of the National Real-Time Air Quality Reporting System

by the China National Environmental Monitoring Center. During the observation in Hefei, hourly PM

concentration data published by the Department of Ecology and Environment of Anhui Province are used

to compare the lidar observation and surface aerosol concentration measured by WIBS.

The real-time temperature and relative humidity are observed by a weather station (Davis, Wireless

130   Vantage Pro2 Plus). Rainrate is monitored by a laser disdrometer (OTT, Parsivel2) and visibility is

measured using a visibility sensor (Vaisala, PWD50). These instruments are located on the rooftop of the

School of Earth and Space Science building.

2.3. WIBS data measurements and processing

The WIBS uses light scattering and fluorescence spectroscopy to detect up to five parameters of every

135   interrogated particle including particle size, asphericity factor (AF), and fluorescence intensity in 3

fluorescent channels. Particle size and AF are derived from the elastic light scattering of aerosol particles

irradiated by a 635 nm diode laser, where particle size ranges from 0.5 μm to 30 μm and AF ranges from

0–100. In theory, perfectly spherical particles exhibit an AF value of 0, whereas an AF value close to

100 indicates a fiber-like particle. An elastic light scattering signal beyond the threshold will trigger two

140   xenon flashlamps to emit light at wavelengths of 280 nm and 370 nm, respectively, to excite the

fluorescence emission of interrogated particles. The fluorescence signal will be recorded in two

Atmospheric
Measurement
Techniques
Discussions

Open Access

EGU

wavelength bands (310–400 nm and 420–650 nm). These configurations result in three fluorescence detection channels with different excitation and detection wavelength bands: The FL1 channel with excitation at 280 nm and detection in the 310–400 nm band, the FL2 channel with excitation at 280 nm,

145 and detection in the 420–650 nm band and the FL3 channel with excitation at 370 nm and detection in the 420–650 nm band.

A set of fluorescent thresholds is used to discriminate between fluorescent (marked as 'fluor' in the following section) and non-fluorescent (marked as 'nonfluor' in the following section) aerosol particles. Any particle whose fluorescence intensity on any one of the fluorescence channels (FL1, FL2, or FL3)

150 exceeds its threshold will be regarded as fluorescent. In this paper, the fluorescent threshold $E_{Threshold}$ in each channel is defined as

$$E_{Threshold} = E + 3\sigma \ , \tag{2}$$

Where E is the signal baseline and σ is the standard deviation of the signal in each channel. The above two parameters are calculated from the result of the WIBS 'Forced Trigger' (FT) working process.

155 During the FT process, the xenon flashlamps are triggered to fire continuously and fluorescent signals in three channels are recorded in the absence of sampled particles.

Using the threshold strategy in Perring et al.(2015), whole fluorescent particles can be further categorized into seven types of fluorescent particles (A, B, C, AB, AC, BC, or ABC). The characteristics of these types of fluorescent particles and non-fluorescent particles are counted. It should be noted that due to the

160 limitation of xenon flashlamp recharge time, some particles which meet the trigger conditions may not be interrogated by flashlamp during the sampling procedure and only their particle sizes and asphericity factors are recorded. These non-excited particles are picked randomly during the sampling procedure regardless of their properties. When calculating the number concentrations (marked as N_{xx}, 'xx' refers to an aerosol type of aerosols) of excited particles (including fluorescent particles), compensation will be

165 factored in by multiplying the ratio of the concentration of total particles to the concentration of excited particles.

To better understand the sources of different types of aerosol particles and minimize the effect of atmospheric boundary layer development, the number fractions to total particles of each type of aerosol particle (i.e. N_{xx}/N_{Total}, marked as $F_{Total}(xx)$) and the number fractions to whole fluorescent particles

170 of each type for fluorescent aerosol particles (i.e. N_{xx}/N_{Fluor}, marked as $F_{Fluor}(xx)$) are investigated. During observation, the variations of each type of aerosol particle in their size and asphericity factor

distribution can also predict some atmospheric events such as hygroscopic growth and dust transport. In this paper, the count mean diameters (marked as $Mean\ D_{xx}$) and count mean asphericity factors (marked as $Mean\ AF_{xx}$) of each investigated type of aerosol particle are used to present their variations in their

175   size distribution and AF distribution.

During observation, a WIBS instrument (NEO model) is located in a room on the top floor of the School of Earth and Space Science building. The atmospheric aerosols are sampled by WIBS through a sampling tube extending about 2 m outside the building. The FT process is performed every 8 hours during the observation and the thresholds at a specific time are determined by the linear interpolation of two adjacent

180   FT procedure results. Although the lower limit for particle size measurement is 0.5 μm, only particles with a size larger than 0.8 μm are discussed in this paper for consistency with other studies and excluding potential interferents. The following ten types of aerosol particles are counted every 30 min: total particles, non-fluorescent particles, seven types of fluorescent particles, and whole fluorescent particles.

2.4. Backward trajectory analysis using the HYSPLIT model

185   To identify aerosol sources and the transport path, the HYSPLIT model (Stein et al., 2015) is used in this study. The HYSPLIT model is configured to use meteorological data from the Global Data Assimilation System (GDAS) at a spatial resolution of 1° for performing a 48 h backward trajectory computation.

3. Result and discussion

190   **3.1. Aerosol transport event on 13 March**

3.1.1. Lidar and in situ observation

Figure 1(a–e) shows the time-height cross-section of the attenuated backscatter coefficient, Doppler spectral width, and wind vector over Hefei. The difference in wind direction between wind at high altitude and near the surface can be seen at 0:00. With the downward development of wind at high altitude,

195   the wind near the surface changes direction from south to north at about 3:30. At the same time, an external aerosol layer occurs at a height of 1.5 km accompanied by high-speed horizontal wind (~10 m s^{-1}). When the external aerosol layer reaches the ground along with the high-speed wind at 7:30, the attenuated backscatter coefficient near the surface shows enhancement, and significant increases in local

PM concentrations can be observed (Fig. 1(f)) in the meantime. After 9:00, the detection range of lidar

200   drops sharply to about 500 m due to strong optical attenuation near the surface. The Lidar signals at the

largest detection range show stronger backscatter and much broader Doppler spectral width compared to

that near the surface layer during this period. The above phenomena indicate that a low-altitude cloud

layer with a high concentration of aerosol moves to Hefei after 9:00.

It should be noted that PM_{10} (Fig. 1(f)) reaches its maximum concentration of 122 μg m^{-3} and starts to

205   decrease at 10:00, 1 hour after the low-altitude cloud layer is observed by the lidar system. In contrast to

PM_{10}, the $PM_{2.5}$ concentration sharply increases after 10:00 and reaches a maximum of 110 μg m^{-3} at

12:00, which is also the highest $PM_{2.5}$ concentration record between 11–20 March. When the cloud layer

stays at the low-altitude layer between 9:00 and 21:00, local weather conditions (Fig. 1(i)) show high

humidity (78 %–89 %) and low temperatures (6 ℃–13 ℃), which inhibit aerosol diffusion but favor the

210   accumulation of local aerosols and hygroscopic growth of small particles. As such, the increase in

particulate matter concentration from 7:00 to 9:00 is mainly attributed to external aerosol transport. The

decrease in PM_{10} after 10:00 is attributed to wet deposition caused by high humidity, while the increase

in $PM_{2.5}$ concentration between 10:00 and 12:00 results from external aerosol transport, local aerosol

emission, accumulation, and hygroscopic growth. After 12:00, the horizontal wind near the surface

215   accelerates and a precipitation event occurs from 15:00–18:00 (Fig. 1(j)). These two factors contribute

to local aerosol diffusion and removal and explain the decrease in local PM concentrations after 12:00.

WIBS data (Fig. 1(g)) show that local aerosol number concentration significantly increases from 8:00,

and reaches its maximum number concentration of 11.93 cm^{-3} at 10:00, which is the highest number

concentration observed by WIBS between 11–20 March. The size distribution variation (Fig. 1(h))

220   reveals the greatest increase in aerosol particles comes from sub-micron particles. The different behavior

of PM data and WIBS data may be due to the difference in observation location and monitoring method.

3.1.2.   Categorized WIBS data

WIBS statistics on 13 March are shown in Fig. 2. N_A, N_B, N_C and N_{BC} sharply increase from 8:00, 30

minutes after the high-speed wind at high altitude reaches the ground, and finally reach their peak at

225   about 10:00, which is consistent with the N_{Toatal}, $N_{NonFluor}$, N_{Fluor} and the PM_{10} concentration (Fig.

1 (f)). Accompanied with their increasing number concentration, these types of aerosol particles except

Type BC exhibited a sharp decrease in their $Mean\ D$ and $Mean\ AF$, and reach their daily minimum

Atmospheric
Measurement
Techniques

Discussions

Open Access

EGU

$Mean\ D$ during this period. However, Type AB and Type ABC particles have different time variation trends from the above-mentioned fluorescent particles: N_{AB} and N_{ABC} both start to increase at about

230   3:30 when the wind near the surface changes (Fig. 2(b)) and they reach their peak at about 7:00–8:00, causing $F_{Fluor}(AB)$ and $F_{Fluor}(ABC)$ to increase from 1.5 % and 6.8 % to their maximum of 6.2 % and 16.3 % respectively. Meanwhile $Mean\ D_{AB}$ and $Mean\ D_{ABC}$ reach their daily minimum but no obvious trends are observed in their $Mean\ AF$. Moreover, there are two other types of particles showing unique trends: Type AC particles shows an obscure time variation due to their extremely low concentration and

235   are excluded from the further discussion; Type BC particles reach their maximum concentration at 10:00 but $Mean\ D_{BC}$ decreases only very slightly at this time, reaches the daily minimum value at 16:00 during the rainfall event and a second minimum value at 5:30 when N_{AB} and N_{ABC} increase.

The differences in these types of fluorescent aerosols reveal that the increased aerosols between 7:30–10:00 have different sources from those between 3:30–7:30. Type AB, ABC, and a tiny fraction of Type

240   BC aerosols reach Hefei from the north after 3:30 when the wind near the surface changes its direction. The majority of these are in the fine mode so their mean diameters decrease during this period. After 7:30, as the external aerosols at high altitude are transported to the ground with high-speed winds, most types of aerosols have not only increased concentrations but also decreased $Mean\ D$ and $Mean\ AF$. Considering the high humidity (> 80 %) and low temperature on that day which favors hygroscopic

245   growth, their decreased $Mean\ D$ and $Mean\ AF$ can be explained by the hygroscopic growth of transported particles whose origin sizes are below the detection range. Due to hygroscopic growth or aggregation and the resulting deposition of large-size particles, Type AB and ABC aerosols have increased $Mean\ D$ but decreased N during this period. After 12:00, all types of aerosol particles decrease sharply in concentration as the horizontal wind accelerates.

250   Moreover, N_A, N_{AB}, and N_{ABC} and F_{Fluor} began to increase after a drizzle event observed at 15:00 (Fig. 2(i)). This phenomenon is similar to the previous observation in Beijing (Yue et al., 2016) and can be explained by the wet discharge after rainfall.

3.1.3.   Transport path and transported bioaerosol types

HYSPLIT backward trajectory results (Fig. 3) show the difference in direction between winds near the

255   surface and at high altitude. The wind near the surface has a southerly direction between 0:00 and 4:00. However, the wind at high altitude has a different direction when traveling over Hefei and changes

Atmospheric
Measurement
Techniques
Discussions

Open Access

EGU

direction earlier than the wind near the surface. At 4:00, the wind direction at high altitude changes from the southeast to the north while the wind on the surface is still southerly. At 8:00, the local wind near the surface changes to a northerly direction that is consistent with the wind at high altitude. At 12:00, when

260   the $PM_{2.5}$ concentration in Hefei reaches its maximum, both the wind near the surface and at high altitude show a transport path passing several coastal cities such as Hangzhou, Ningbo, and Shanghai, carrying wet airflows and pollutants to Hefei.

Laboratory tests (Hernandez et al., 2016) show fungal spores and bacterial aggregates contribute to Type AB particles in WIBS data, while fungi present a mixture of Type A, AB, and ABC particles. Although

265   pollen fragments are often categorized as Type ABC, the increasing concentration of Type AB and ABC particles, as well as the decline in mean diameter during the transport event, means that the transported bioaerosols are more likely to be fungi or bacteria aggregates. Their increase after the change in wind direction and the low speed of the wind near the surface during this period indicates that the transported bioaerosols most likely come from the nearby rural area north of Hefei.

270   **3.2. Aerosol transport event on 16–17 March**

3.2.1.   Lidar and in situ observation

Figure 4(a–e) shows the lidar observation results during 16–17 March. A developing cloud layer that extends downwards can be seen on 16 March. This cloud layer reaches its lowest height of 2 km at 22:00 on 16 March before moving upward and disappearing. During this period, a high-speed horizontal wind

275   is observed in the upper cloud layer with a high vertical speed (~2 m s^{-1}). A broadened Doppler spectral width is also observed underneath the cloud. These characteristics are the same as that of a precipitation phenomenon while no rainfall is recorded on the ground (Fig. 4(j)). These observations indicate a virga event, during which the ice crystal beneath the cloud layer results in enhanced lidar backscatter. During the virga event, the wind at high altitude migrates downward, causing the southeast wind near the surface

280   to weaken and finally change to the northwest direction at 01:30 on 17 March, making it consistent with the wind at high altitude. Meanwhile, an external aerosol layer can be observed at a height of about 0.5–1.5 km, which may be from the accumulation of aerosol that originally acted as ice nuclei during the virga event. Due to the mixing of the local aerosol and external aerosol contained in the wind at high altitude and the increase in $PM_{2.5}$ and PM_{10} concentration (Fig. 4(f)), the total particle number

285   concentration of WIBS (Fig. 4(g)) is observed. The ground observation result shows a maximum $PM_{2.5}$

concentration (Fig. 4(f)) of 71 µg m^{-3} at 10:00 on 17 March, which is the second-highest peak concentration between 11–20 March. WIBS data show a higher fraction of coarse particles at this time than that during the event on 13 March. Under the influence of solar radiation, local temperature and relative humidity show a sharp increase and decrease respectively (Fig. 4(i)). The Doppler spectral width

290   profile (Fig. 4(b)) shows that compared to values on 16 March, the convective boundary layer on 17 March has a much higher maximum height of more than 2 km at about 15:30 which favors the diffusion of aerosol. The aerosol concentrations decrease sharply under strong diffusion after 10:00 on 17 March.

3.2.2.   Categorized WIBS data

The statistical results of WIBS data between 16–17 March are shown in Fig. 5. The number concentration

295   of each type of aerosol increases during the transport event (Fig. 4). Their maximum concentrations are all observed at about 8:30, which is consistent with the time of maximum PM$_{10}$ concentration (Fig. 4(f)). Despite these increases, the $F_{Fluor}(BC)$ shows a significant drop from 48.0 % at 6:00 to 41.2 % at 8:30. On the contrary, $F_{Fluor}(A)$, $F_{Fluor}(AB)$ and $F_{Fluor}(ABC)$ increase from 1.6 %, 1.0 % and 4.8 % at 6:00 to 4.7 %, 2.4 % and 8.7 % at 8:30 on 17 March respectively. These changes that occur in a short amount

300   of time reveal that the transport of aerosols not only leads to high PM$_{10}$ and PM$_{2.5}$ concentrations but also a higher fraction of fluorescent biological aerosols.

The variation in mean diameters (Fig. 5) revealed that Type B, C, and BC particles share the same variation trend with non-fluorescent and total particles. Their $Mean\ D$ keep decreasing when their N increase slightly between 1:30 and 6:00 on 17 March, followed by increases in both their $Mean\ D$ and

305   N until 8:30. The phenomenon indicates that the increase in N consists of two stages. From 1:30 to 6:00, the increased number of aerosol particles are mainly in fine mode; but from 6:00 to 8:30, the increased number of particles have higher fractions of coarse mode. However, this two-stage variation is not observed in all Type FL-1 particles (Type A, AB, AC, ABC). The Type FL-1 particles do not show increases in number concentrations during stage 1 but show sharp increases in stage 2. And their $Mean\ D$

310   show no apparent variation (Fig. 5 (d) (g) (h) and (j)) during the 2 stages. It can be explained that from 1:30 to 6:00 on 17 March the increase in particle concentrations mainly resulted from the local aerosol accumulation and possible hygroscopic growth caused by rising humidity and low turbulence intensity (Fig. 4(b)). After 6:00 on 17 March, turbulence intensity began to increase as sunrise occurred, which inhibit local aerosol accumulation increased particles are dominated by transported external aerosols in

Atmospheric
Measurement
Techniques
Discussions

Open Access

EGU

315   which there were a higher fraction of particles in the coarse mode. The sharp increase in N of Type FL-1 particles indicates their main source is the transported external aerosols.

3.2.3.   Transport path and transported bioaerosol types

The backward trajectory results shown in Fig. 6 reveal that during the transport event, the wind near the surface changes direction in Hefei from the southeast at 22:00 on 16 March to the west at 6:00 on 17

320   March, which is consistent with lidar observation shown in Fig. 4(d). The difference in direction between wind near the surface and at high altitude over Hefei at 10:00 on 17 March is supported by lidar observation (Fig. 4 (d)) and can be explained by local turbulence after sunrise. Trajectory results show that the air mass at both levels passes through the Dabie Mountains west of Hefei which can be a source of bioaerosols. During the event on 16–17 March, the increased amount of fluorescent aerosols have

325   similar fluorescent types and characteristics to that in the event on 13 March. Therefore, the transported bioaerosols can be fungi or bacteria aggregates from the Dabie Mountains.

3.3. Aerosol transport event on 19 March

3.3.1.   Lidar and in situ observation

As portrayed in Fig. 7 (a–e), an external aerosol layer accompanies the high-speed northwest wind (~20

330   m s-1) and is observed at a height of 2–3 km at 2:00. It moves down to the ground at 5:00. Meanwhile, the wind near the surface changes direction from southwest to northeast, which is consistent with the wind at high altitude. Strong wind shear at this moment broadens the Doppler spectral width shown in Fig. 7(b). After 5:00, with the development of convection, the thermal mixing layer is elevated, which favors surface aerosol diffusion. An entrainment layer with relatively low wind speed and strong

335   backscatter occurred above the mixing layer after the transport of external aerosol and moved upward to above 2 km at 12:00. After 12:00, interference between the entrainment layer and the thermal mixing layer can be observed. PM_{10} concentrations (Fig. 7 (f)) show a significant increase from 111 $\mu g\ m^{-3}$ at 7:00 to 524 $\mu g\ m^{-3}$ at 10:00 with the enhancement of attenuated backscatter coefficient near the surface. This is the highest PM_{10} record between 11–20 March, but no obvious increase in $PM_{2.5}$ concentration is

340   observed. WIBS data (Fig. 7 (g) (h)) show that particles in coarse mode are most abundant during this period. Temperature is rising and humidity decreasing (Fig 7. (i)) while PM_{10} is increasing, which inhibits hygroscopic growth of particles and accumulation. As such, it is believed that the PM_{10} on 19 March

mainly comes from external aerosols rather than local aerosols. After sunrise, with an increase in solar

radiation, the PBL height rises and the PM concentration began to decrease after 10:00 under the

345   influence of aerosol diffusion and dry deposition.

3.3.2.   Categorized WIBS data

Figure 8 reveals that as the external aerosol reaches the ground (Fig. 7(a)), $Mean\ D$ and $Mean\ AF$ of

all types of fluorescent aerosol particles increase at different degrees from 6:00 on 19 March, indicating

that the external aerosol layer is dominated by non-spherical aerosol particles in coarse mode, which are

350   most likely mineral dust. However as portrayed in Fig. 8(i), N_{BC} significantly decreases, causing

$F_{Fluor}\ (BC)$ to decrease from 58.7 % at 6:00 to 36.33 % at 9:00 while all other types of fluorescent

particles exhibit an increase in their N.

The sharp decrease of N_{BC} indicates a much smaller fraction of type BC in external fluorescent aerosols

than that in local aerosols. Besides, $F_{Total}\ (Fluor)$ decreases rapidly from 45.4 % at 6:00 to 29.4 % at

355   9:00 due to dust transport (Fig. 8(b)). However, $F_{Total}\ (A)$ and $F_{Total}\ (AB)$ increase from 0.72 % and

0.46 % at 6:00 to 1.43 % and 0.88 %, in contrast with the behavior of all other fluorescent particles (Fig.

8 (d) and (g)). It can be inferred that the $(N_A + N_{AB})/N_{BC}$ is higher in external aerosols than that in local

aerosols. Previous research (Yue et al., 2016, 2019) regards Type FL1 (Type A, AB, ABC) particles in

WIBS as protein-like bioaerosols and Type BC as highly oxygenated humic-like substances (HULIS).

360   During long-range transport, Type A particles can be photo-oxidized, contributing to HULIS which can

be categorized as Type BC particles by WIBS. In aged aerosols during long-range transport,

$(N_A + N_{AB})/N_{BC}$ is thought to be lower than that in local aerosols. However, the observation in this

paper shows a completely different result. Considering this is observed during a dust event, it may be

explained that bioaerosol particles can survive under intense solar radiation due to the mechanism of

365   attaching to other large particles. This explanation is supported by the larger size of fluorescent aerosols

in external aerosols.

3.3.3.   Transport path and transported bioaerosol types

The backward trajectory result on 19 March (Fig. 9) shows the wind direction gradually changing near

the surface and at high altitude over Hefei. From 6:00, the direction of the wind near the surface changed

370   from southwest to northeast, which is consistent with the wind at high altitude. At 8:00, the high-altitude

airmass over Hefei shows a new transport path. As the wind at high altitude migrates downwards, the airmass at both heights over Hefei at 10:00 shows similar transport paths. The long-range transport path indicates a high-speed northerly wind, which is consistent with the lidar observation result. The transport path at both heights passes the Gobi desert at the China-Mongolia border, which is one of the main

375   sources of dust storms in East Asia.

Although particles in a larger size are more likely to exhibit a wider fluorescent spectrum range and higher fluorescent intensity (Yue et al., 2019), the 19 March event the increase in large-size particles leads to an increase in Type A and Type AB particles rather than an increase in the fraction of Type ABC particles (Fig 8 (j)). This increase in large-sized Type A and AB particles may result from bacteria

380   attached to the dust.

4.   Conclusion

In this paper, three aerosol transport events between 11–20 March 2020 in Hefei were investigated. The results of a coherent Doppler wind lidar and a bioaerosol sensor WIBS, local meteorological parameters, local PM concentrations, and the HYSPLIT backward trajectory model are used during the investigation.

385   The analysis result is summarized as follows.

During all three transport events, differences between the directions for wind at high altitude and near the surface and the downward migration of wind at high altitude were observed. Enhancement in the attenuated backscatter coefficient near the surface was captured as the wind at high altitude reached the ground, and a corresponding surface PM concentration increase was monitored during the events. During

390   the observation, the 13 March and 16–17 March events caused the highest and second-highest $PM_{2.5}$ concentration record respectively, and PM_{10} concentration reached the highest record during the 19 March event.

During the above three transport events, seven types of fluorescent particles, as well as non-fluorescent particles, are categorized and counted using WIBS data. The fractions to total particles and the fractions

395   to fluorescent particles for Type AB and Type ABC particles increased during the 13 March and 16–17 March events. In the 19 March event, the fraction to total particles of Type A and Type AB particles increased while all other types of fluorescent particles showed a decreasing trend. These phenomena proved the influence of transported external bioaerosols. WIBS statistics and backward trajectory results

400   showed that possible origins for external bioaerosols are fungi or bacterial aggregations originating from rural areas in the north of Hefei during the 13 March event, fungi or bacterial aggregations originating from Dabie Mountains in the west of Hefei in the 16–17 March event, dust-attached bacteria originating from Gobi Desert in China-Mongolia border in the 19 March event.

In this paper, the impact of external bioaerosol transport on local aerosol composition is observed and the potential of real-time monitoring of transport of fluorescent bioaerosols is proven using the UV-LIF

405   based on-line measurement instrument accompanied with ground-based lidar. The time resolution compared with traditional offline bioaerosol measurement is improved. The parameters in aerosol monitoring are expanded by introducing AF and fluorescence intensity, which contribute to a further understanding of bioaerosol transport.

Data availability. The GDAS data in HYSPLIT backward trajectory are publicly available from the

410   NOAA website at https://www.ready.noaa.gov/hypub-bin/trajasrc.pl. All other data in this study are available from the authors upon request.

Author contributions. JY performed the lidar observations. TW downloaded the local meteorological data and derived the parameters needed from the raw lidar data. DT performed the WIBS observations, HYSPLIT backward trajectories, carried out the data analysis, prepared the figures, and wrote the original

415   draft. All authors contributed to the interpretation of discussion data, manuscript reviewing, and editing.

Competing interests. The authors declare that they have no conflict of interest.

References

Banakh, V. A., Brewer, A., Pichugina, E. L. and Smalikho, I. N.: Measurements of wind velocity and direction with coherent Doppler lidar in conditions of a weak echo signal, Atmos. Ocean. Opt., 23(5),

420   381–388, doi:10.1134/S1024856010050076, 2010.

Cheng, B., Yue, S., Hu, W., Ren, L., Deng, J., Wu, L. and Fu, P.: Summertime fluorescent bioaerosol particles in the coastal megacity Tianjin, North China, Sci. Total Environ., 723, 137966, doi:10.1016/j.scitotenv.2020.137966, 2020.

Crawford, I., Lloyd, G., Herrmann, E., Hoyle, C. R., Bower, K. N., Connolly, P. J., Flynn, M. J., Kaye,

425   P. H., Choularton, T. W. and Gallagher, M. W.: Observations of fluorescent aerosol-cloud interactions

in the free troposphere at the High-Altitude Research Station Jungfraujoch, Atmos. Chem. Phys., 16(4), 2273–2284, doi:10.5194/acp-16-2273-2016, 2016.

Daly, S. M., O'Connor, D. J., Healy, D. A., Hellebust, S., Arndt, J., McGillicuddy, E., Feeney, P., Quirke, M., Wenger, J. and Sodeau, J.: Investigation of coastal sea-fog formation using the WIBS (wideband

430   integrated bioaerosol sensor) technique, Atmos. Chem. Phys., 19(8), 5737–5751, doi:10.5194/acp-19-5737-2019, 2019.

Fang, Z., Yang, H., Cao, Y., Xing, K., Liu, D., Zhao, M. and Xie, C.: Study of persistent pollution in hefei during winter revealed by ground-based LiDAR and the CALIPSO satellite, Sustain., 13(2), 1–15, doi:10.3390/su13020875, 2021.

435   Feeney, P., Rodríguez, S. F., Molina, R., McGillicuddy, E., Hellebust, S., Quirke, M., Daly, S., O'Connor, D. and Sodeau, J.: A comparison of on-line and off-line bioaerosol measurements at a biowaste site, Waste Manag., 76, 323–338, doi:10.1016/j.wasman.2018.02.035, 2018.

Fennelly, M. J., Sewell, G., Prentice, M. B., O'Connor, D. J. and Sodeau, J. R.: Review: The use of real-time fluorescence instrumentation to monitor ambient primary biological aerosol particles (PBAP),

440   Atmosphere (Basel)., 9(1), doi:10.3390/atmos9010001, 2017.

Fernández-Rodríguez, S., Tormo-Molina, R., Lemonis, N., Clot, B., O'Connor, D. J. and Sodeau, J. R.: Comparison of fungal spores concentrations measured with wideband integrated bioaerosol sensor and Hirst methodology, Atmos. Environ., 175(May 2017), 1–14, doi:10.1016/j.atmosenv.2017.11.038, 2018.

Gabey, A. M., Stanley, W. R., Gallagher, M. W. and Kaye, P. H.: The fluorescence properties of aerosol

445   larger than 0.8 μ in urban and tropical rainforest locations, Atmos. Chem. Phys., 11(11), 5491–5504, doi:10.5194/acp-11-5491-2011, 2011.

Healy, D. A., Huffman, J. A., O'Connor, D. J., Pöhlker, C., Pöschl, U. and Sodeau, J. R.: Ambient measurements of biological aerosol particles near Killarney, Ireland: A comparison between real-time fluorescence and microscopy techniques, Atmos. Chem. Phys., 14(15), 8055–8069, doi:10.5194/acp-14-

450   8055-2014, 2014.

Hernandez, M., Perring, A. E., McCabe, K., Kok, G., Granger, G. and Baumgardner, D.: Chamber catalogues of optical and fluorescent signatures distinguish bioaerosol classes, Atmos. Meas. Tech., 9(7), 3283–3292, doi:10.5194/amt-9-3283-2016, 2016.

Ho, H. M., Rao, C. Y., Hsu, H. H., Chiu, Y. H., Liu, C. M. and Chao, H. J.: Characteristics and
455   determinants of ambient fungal spores in Hualien, Taiwan, Atmos. Environ., 39(32), 5839–5850,
doi:10.1016/j.atmosenv.2005.06.034, 2005.

Hua, N. P., Kobayashi, F., Iwasaka, Y., Shi, G. Y. and Naganuma, T.: Detailed identification of desert-
originated bacteria carried by Asian dust storms to Japan, Aerobiologia (Bologna)., 23(4), 291–298,
doi:10.1007/s10453-007-9076-9, 2007.

460   Huang, T., Yang, Y., O'Connor, E. J., Lolli, S., Haywood, J., Osborne, M., Cheng, J. C. H., Guo, J. and
Yim, S. H. L.: Influence of a weak typhoon on the vertical distribution of air pollution in Hong Kong: A
perspective   from   a   Doppler   LiDAR   network,   Environ.   Pollut.,   276,   116534,
doi:10.1016/j.envpol.2021.116534, 2021.

Jeon, E. M., Kim, H. J., Jung, K., Kim, J. H., Kim, M. Y., Kim, Y. P. and Ka, J. O.: Impact of Asian dust
465   events on airborne bacterial community assessed by molecular analyses, Atmos. Environ., 45(25), 4313–
4321, doi:10.1016/j.atmosenv.2010.11.054, 2011.

Jeon, E. M., Kim, Y. P., Jeong, K., Kim, I. S., Eom, S. W., Choi, Y. Z. and Ka, J. O.: Impacts of Asian
dust   events   on   atmospheric   fungal   communities,   Atmos.   Environ.,   81,   39–50,
doi:10.1016/j.atmosenv.2013.08.039, 2013.

470   Jia, M., Yuan, J., Wang, C., Xia, H., Wu, Y., Zhao, L., Wei, T., Wu, J., Wang, L., Gu, S. Y., Liu, L., Lu,
D., Chen, R., Xue, X. and Dou, X.: Long-lived high-frequency gravity waves in the atmospheric
boundary layer: Observations and simulations, Atmos. Chem. Phys., 19(24), 15431–15446,
doi:10.5194/acp-19-15431-2019, 2019.

Ma, Y., Wang, Z., Yang, D., Diao, Y., Wang, W., Zhang, H., Zhu, W. and Zheng, J.: On-line
475   measurement of fluorescent aerosols near an industrial zone in the Yangtze River Delta region using a
wideband   integrated   bioaerosol   spectrometer,   Sci.   Total   Environ.,   656,   447–457,
doi:10.1016/j.scitotenv.2018.11.370, 2019.

Maki, T., Puspitasari, F., Hara, K., Yamada, M., Kobayashi, F., Hasegawa, H. and Iwasaka, Y.:
Variations in the structure of airborne bacterial communities in a downwind area during an Asian dust
480   (Kosa) event, Sci. Total Environ., 488–489(1), 75–84, doi:10.1016/j.scitotenv.2014.04.044, 2014.

Maki, T., Hara, K., Kobayashi, F., Kurosaki, Y., Kakikawa, M., Matsuki, A., Chen, B., Shi, G., Hasegawa,
H. and Iwasaka, Y.: Vertical distribution of airborne bacterial communities in an Asian-dust downwind
area, Noto Peninsula, Atmos. Environ., 119, 282–293, doi:10.1016/j.atmosenv.2015.08.052, 2015.

O'Connor, E. J., Illingworth, A. J. and Hogan, R. J.: A technique for autocalibration of cloud lidar, J.

485   Atmos. Ocean. Technol., 21(5), 777–786, doi:10.1175/1520-0426(2004)021<0777:ATFAOC>2.0.CO;2,

2004.

Pentikäinen, P., James O'connor, E., Juhani Manninen, A. and Ortiz-Amezcua, P.: Methodology for

deriving the telescope focus function and its uncertainty for a heterodyne pulsed Doppler lidar, Atmos.

Meas. Tech., 13(5), 2849–2863, doi:10.5194/amt-13-2849-2020, 2020.

490   Perring, A. E., Schwarz, J. P., Baumgardner, D., Hernandez, M. T., Spracklen, D. V., Heald, C. L., Gao,

R. S., Kok, G., McMeeking, G. R., McQuaid, J. B. and Fahey, D. W.: Airborne observations of regional

variation in fluorescent aerosol across the United States, J. Geophys. Res. Atmos., 120(3), 1153–1170,

doi:10.1002/2014JD022495, 2015.

Petters, M. D. and Kreidenweis, S. M.: A single parameter representation of hygroscopic growth and

495   cloud condensation nucleus activity, Atmos. Chem. Phys., 7(8), 1961–1971, doi:10.5194/acp-7-1961-

2007, 2007.

Qin, K., Wu, L., Wong, M. S., Letu, H., Hu, M., Lang, H., Sheng, S., Teng, J., Xiao, X. and Yuan, L.:

Trans-boundary aerosol transport during a winter haze episode in China revealed by ground-based Lidar

and   CALIPSO   satellite,   Atmos.   Environ.,   141(January   2013),   20–29,

500   doi:10.1016/j.atmosenv.2016.06.042, 2016.

Stein, A. F., Draxler, R. R., Rolph, G. D., Stunder, B. J. B., Cohen, M. D. and Ngan, F.: NOAA's

HYSPLIT Atmospheric Transport and Dispersion Modeling System, Bull. Am. Meteorol. Soc., 96(12),

2059–2077, doi:10.1175/BAMS-D-14-00110.1, 2015.

Tang, K., Huang, Z., Huang, J., Maki, T., Zhang, S., Ma, X., Shi, J., Bi, J., Zhou, T., Wang, G. and Zhang,

505   L.: Characterization of atmospheric bioaerosols along the transport pathway of Asian dust during the

Dust-Bioaerosol 2016 Campaign, Atmos. Chem. Phys., 18(10), 1–41, doi:10.5194/acp-2017-1172, 2017.

Wang, H., Li, Z., Lv, Y., Xu, H., Li, K., Li, D., Hou, W., Zheng, F., Wei, Y. and Ge, B.: Observational

study of aerosol-induced impact on planetary boundary layer based on lidar and sunphotometer in Beijing,

Environ. Pollut., 252, 897–906, doi:10.1016/j.envpol.2019.05.070, 2019.

510   Wei, T., Xia, H., Hu, J., Wang, C., Shangguan, M., Wang, L., Jia, M. and Dou, X.: Simultaneous wind

and rainfall detection by power spectrum analysis using a VAD scanning coherent Doppler lidar, Opt.

Express, 27(22), 31235, doi:10.1364/oe.27.031235, 2019.

Atmospheric
Measurement
Techniques
Discussions

Wei, T., Xia, H., Wu, Y., Yuan, J., Wang, C. and Dou, X.: Inversion probability enhancement of all-fiber CDWL by noise modeling and robust fitting, Opt. Express, 28(20), 29662, doi:10.1364/oe.401054, 2020.

515 Wei, T., Xia, H., Yue, B., Wu, Y. and Liu, Q.: Remote sensing of raindrop size distribution using the coherent Doppler lidar, Opt. Express, 29(11), 17246, doi:10.1364/oe.426326, 2021.

Wu, P. C., Tsai, J. C., Li, F. C., Lung, S. C. and Su, H. J.: Increased levels of ambient fungal spores in Taiwan are associated with dust events from China, Atmos. Environ., 38(29), 4879–4886, doi:10.1016/j.atmosenv.2004.05.039, 2004.

520 Yang, H., Fang, Z., Cao, Y., Xie, C., Zhou, T., Wang, B., Xing, K. and Lolli, S.: Impacts of Transboundary Dust Transport on Aerosol Pollution in the Western Yangtze River Delta Region, China: Insights Gained From Ground-Based Lidar and Satellite Observations, Earth Sp. Sci., 8(3), 1–17, doi:10.1029/2020EA001533, 2021a.

Yang, H., Fang, Z., Xie, C., Cohen, J., Yang, Y., Wang, B., Xing, K. and Cao, Y.: Two trans-boundary

525 aerosol transport episodes in the western Yangtze River Delta, China: A perspective from ground-based lidar observation, Atmos. Pollut. Res., 12(3), 370–380, doi:10.1016/j.apr.2021.01.004, 2021b.

Yang, S., Preißler, J., Wiegner, M., von Löwis, S., Petersen, G. N., Parks, M. M. and Finger, D. C.: Monitoring dust events using doppler lidar and ceilometer in Iceland, Atmosphere (Basel)., 11(12), 1–23, doi:10.3390/atmos11121294, 2020.

530 Yu, X., Wang, Z., Zhang, M., Kuhn, U., Xie, Z., Cheng, Y., Pöschl, U. and Su, H.: Ambient measurement of fluorescent aerosol particles with a WIBS in the Yangtze River Delta of China: Potential impacts of combustion-related aerosol particles, Atmos. Chem. Phys., 16(17), 11337–11348, doi:10.5194/acp-16-11337-2016, 2016.

Yuan, J., Xia, H., Wei, T., Wang, L., Yue, B. and Wu, Y.: Identifying cloud, precipitation, windshear,

535 and turbulence by deep analysis of the power spectrum of coherent Doppler wind lidar, Opt. Express, 28(25), 37406, doi:10.1364/oe.412809, 2020.

Yue, S., Ren, H., Fan, S., Sun, Y., Wang, Z., Fu, P., Ren, L., Song, T., Li, L., Xie, Q., Li, W., Kang, M., Wei, L., Ren, H., Sun, Y., Wang, Z., Ellam, R. M., Kawamura, K., Fu, P., Academy, C., Sciences, A. and Sciences, E.: Springtime precipitation effects on the abundance of fluorescent biological aerosol

540 particles and HULIS in Beijing, Sci. Rep., 6(1), 29618, doi:10.1038/srep29618, 2016.

Yue, S., Ren, L., Song, T., Li, L., Xie, Q., Li, W., Kang, M., Zhao, W., Wei, L., Ren, H., Sun, Y., Wang, Z., Ellam, R. M., Liu, C. Q., Kawamura, K. and Fu, P.: Abundance and Diurnal Trends of Fluorescent

Bioaerosols in the Troposphere over Mt. Tai, China, in Spring, J. Geophys. Res. Atmos., 124(7), 4158–4173, doi:10.1029/2018JD029486, 2019.

545   Ziemba, L. D., Beyersdorf, A. J., Chen, G., Corr, C. A., Crumeyrolle, S. N., Diskin, G., Hudgins, C., Martin, R., Mikoviny, T., Moore, R., Shook, M., Thornhill, K. L., Winstead, E. L., Wisthaler, A. and Anderson, B. E.: Airborne observations of bioaerosol over the Southeast United States using a Wideband Integrated Bioaerosol Sensor, J. Geophys. Res. Atmos., 121(14), 8506–8524, doi:10.1002/2015JD024669, 2016.

550
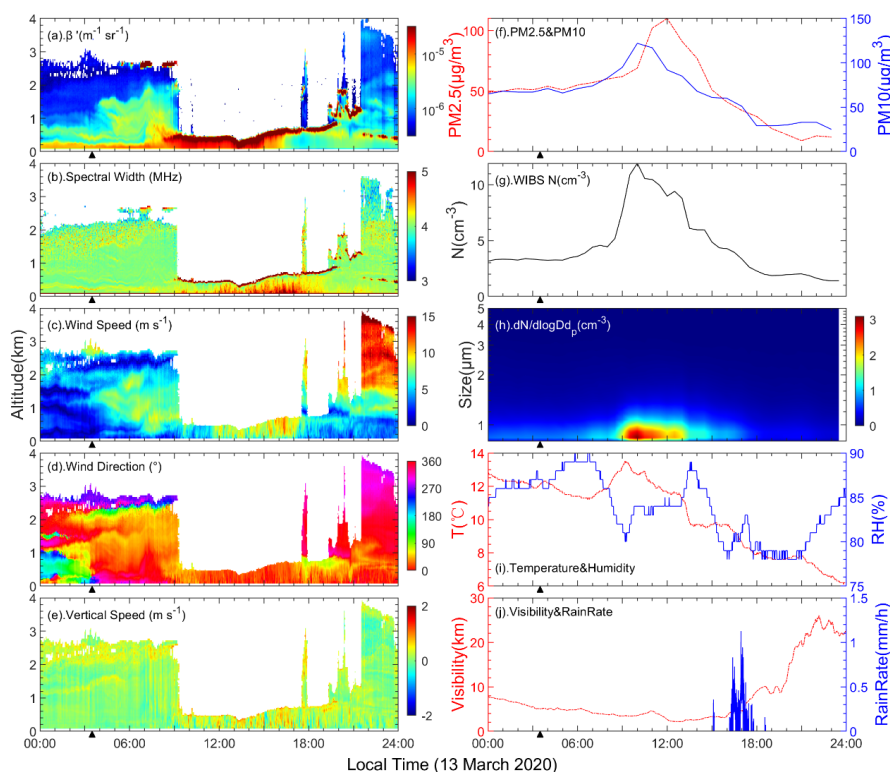
Fig. 1 Left panel: Time-height crosssection of (a) attenuated backscatter coefficient, (b) Doppler spectral width, (c) horizontal wind speed, (d) horizontal wind direction, and (e) vertical wind speed over Hefei observed by CDWL on 13 March 2020. Right panel: simultaneous ground observation results, including (f)
555   **surface hourly particulate matter concentration from local monitor network, (g) number concentration and (h) size distribution of surface total aerosol particles from WIBS, (i) local temperature and humidity, and (j) local visibility and rain rate. The wind direction near the surface changes at about 03:30 and is marked with a triangle symbol.**

20
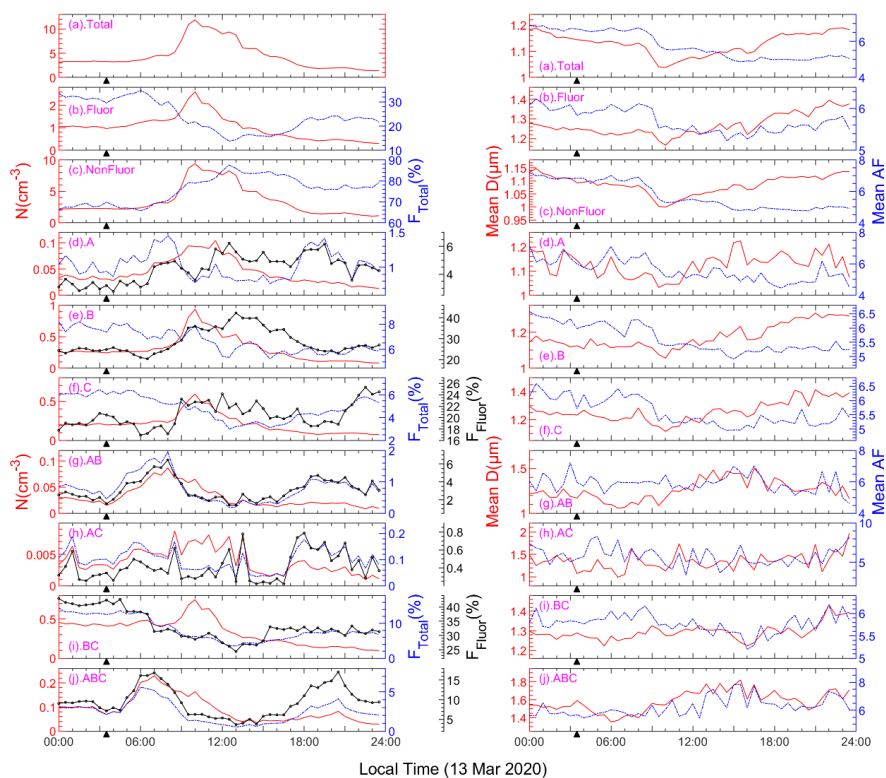
560   **Fig. 2 Left panel: number concentrations (solid red line), number fractions to total particles (blue chain line), and number fractions to fluorescent particles (black solid line with point marker) of the investigated particle types. Right panel: Count mean particle diameter (solid red line) and count mean asphericity factor (blue chain line) of investigated particles measured by WIBS on 13 March 2020. The direction of the wind near the surface changes at about 03:30 and is marked with a triangle symbol.**
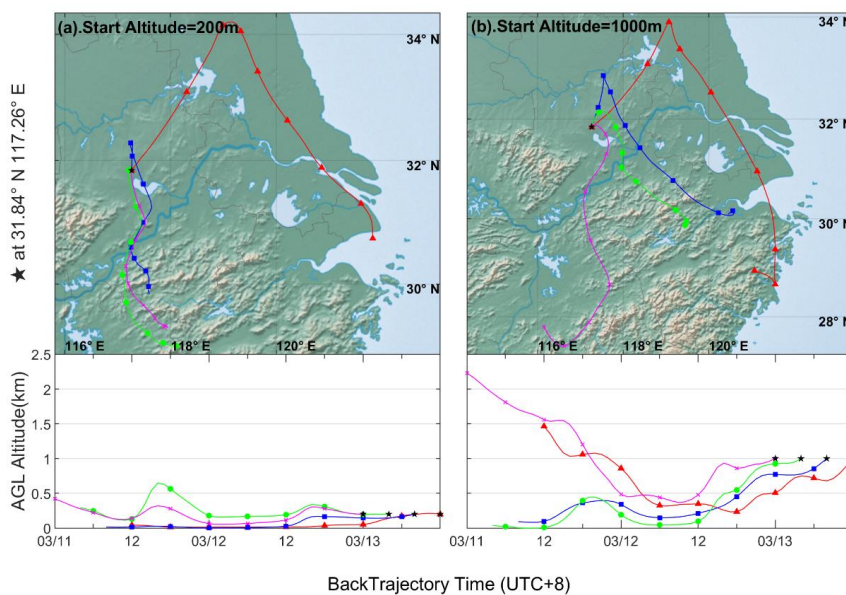
Fig. 3 The 48 h HYSPLIT backward trajectory result calculated at 0:00 (magenta line with cross marker), 4:00 (green line with diamond marker), 8:00 (blue line with square marker), and 12:00 (red line with triangle marker) on 13 March 2020 (UTC+8). Terminal points are marked every 6 hours. The starting location is set as 200 m (left panel) and 1000 m (right panel) over Hefei. The map data used in this figure are from Natural Earth.
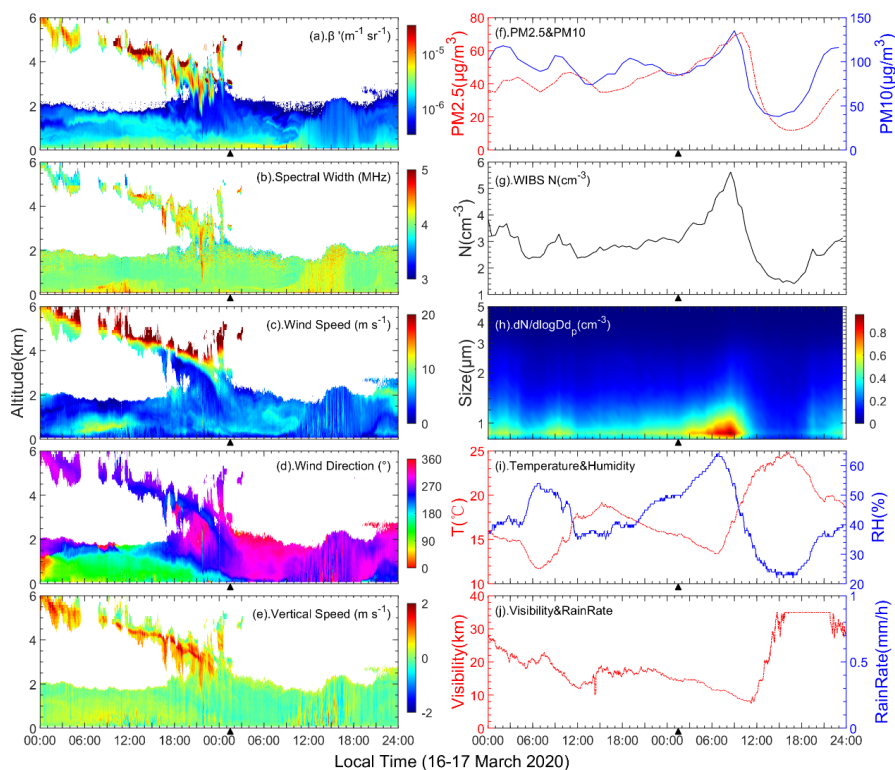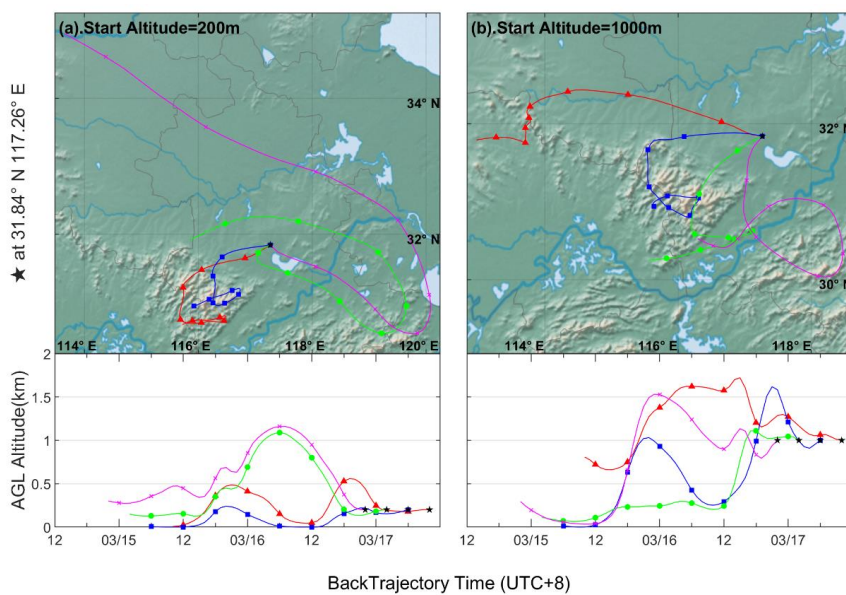
Fig. 4 Left panel: Time-height crosssection of (a) attenuated backscatter coefficient, (b) Doppler spectral width, (c) horizontal wind speed, (d) horizontal wind direction, and (e) vertical wind speed over Hefei observed by CDWL between 16–17 March 2020. Right panel: simultaneous ground observation results, including (f) surface hourly particulate matter concentration from local monitor network, (g) number concentration and (h) size distribution of surface total aerosol particles from WIBS, (i) local temperature and humidity, and (j) local visibility and rain rate. The wind direction near the surface changes at about 01:30 on 17 March and is marked with a triangle symbol.

575
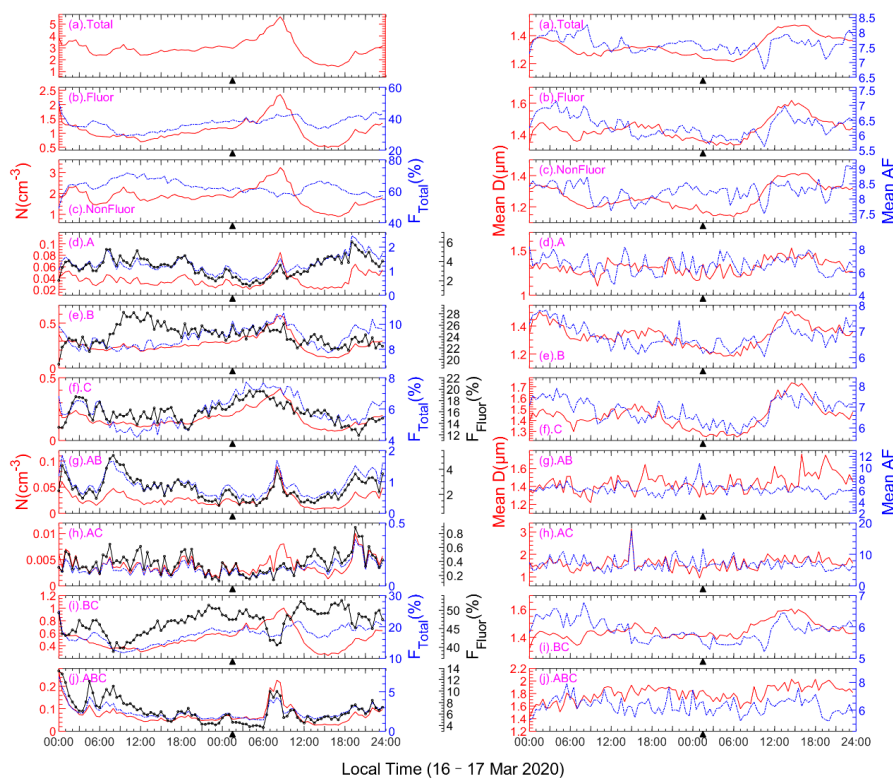
580 **Fig. 5 Left panel: number concentrations (solid red line), number fractions to total particles (blue chain line), and number fractions to fluorescent particles (solid black line with point marker) of investigated particle types. Right panel: Count mean particle diameter (solid red line) and count mean asphericity factor (blue chain line) for investigated particle types measured by WIBS on 16–17 March 2020. The direction of the wind near the surface changes at about 01:30 on 17 March and is marked with a triangle symbol.**
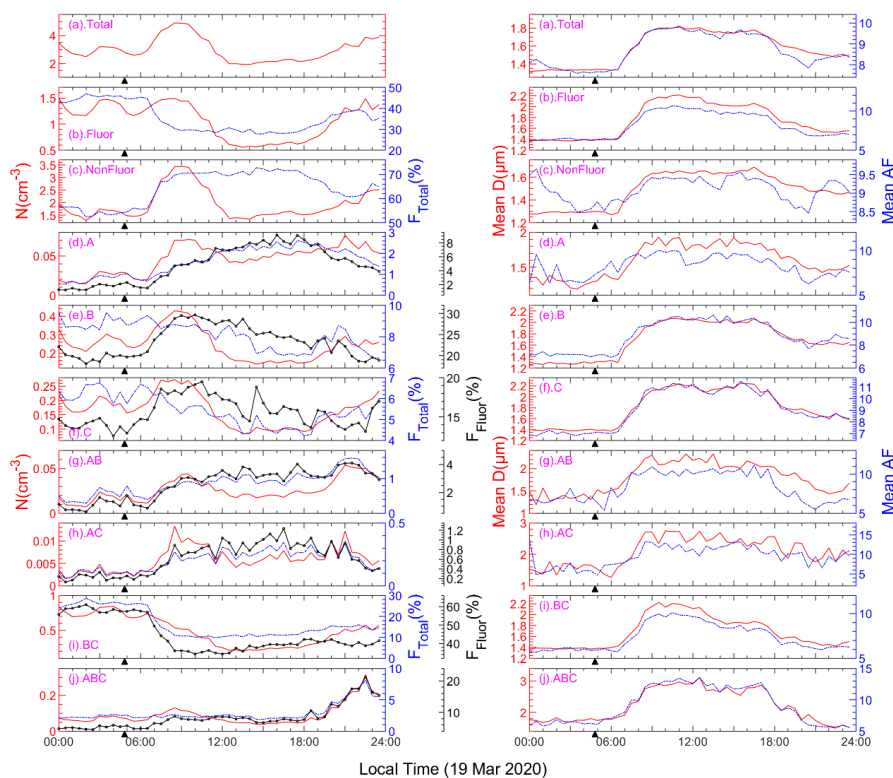
24

Fig. 6 The 48 h HYSPLIT backward trajectory result calculated at 22:00 on 16 March (magenta line with cross marker), 2:00 (green line with diamond marker), 6:00 (blue line with square marker), and 10:00 (red line with triangle marker) on 17 March (UTC+8). The terminal points are marked every 6 hours. The starting location is set as 200 m (left panel) and 1000 m (right panel) over Hefei. The map data used in this figure are from Natural Earth.
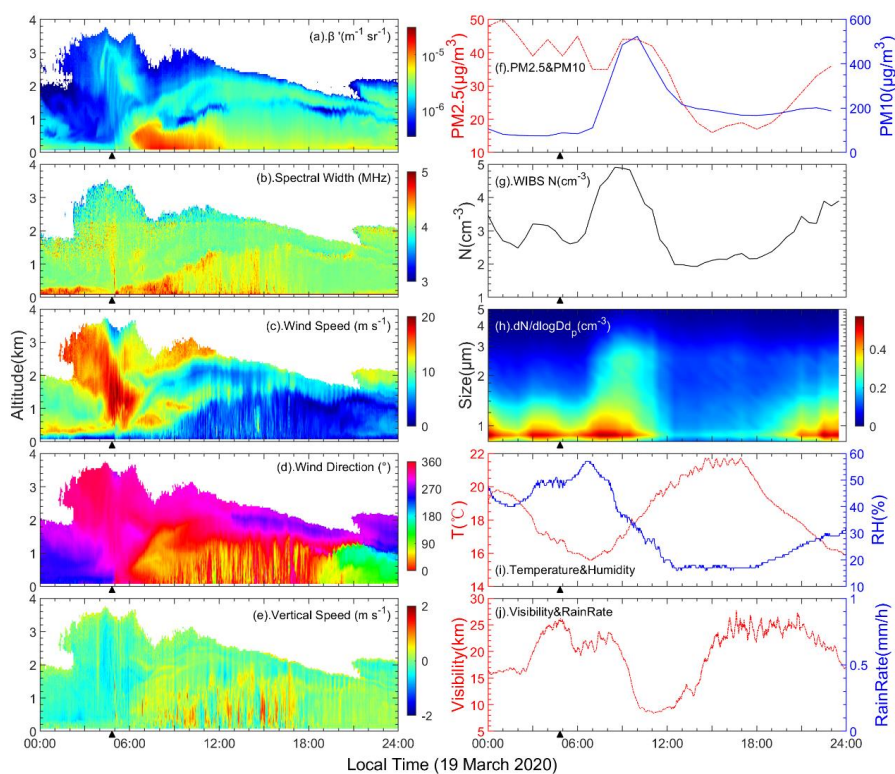
Fig. 7 Left panel: Time-height crosssection of (a) attenuated backscatter coefficient, (b) Doppler spectral width, (c) horizontal wind speed, (d) horizontal wind direction, and (e) vertical wind speed over Hefei observed by CDWL on 19 March 2020. Right panel: simultaneous ground observation results, including (f) surface hourly particulate matter concentration from local monitor network, (g) number concentration and (h) size distribution of surface total aerosol particles from WIBS, (i) local temperature and humidity, and (j) local visibility and rain rate. The wind direction near the surface changes at about 05:00 on 19 March and is marked with a triangle symbol.

595

Fig. 8 Left panel: number concentrations (solid red line), number fractions to total particles (blue chain line), and number fractions to fluorescent particles (solid black line with point marker) of investigated particle types. Right panel: Count mean particle diameter (solid red line) and count mean asphericity factor (blue chain line) of investigated particle types measured by WIBS on 19 March 2020. The wind direction near the surface changed at about 05:00 on 19 March and is marked with a triangle symbol.
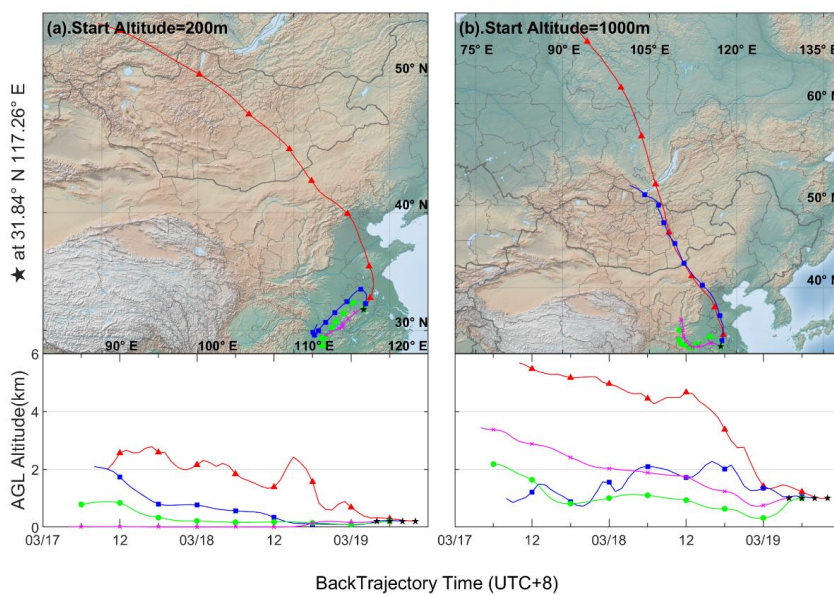
605

Fig. 9 The 48 h HYSPLIT backward trajectory result calculated at 4:00 (magenta line with cross marker), 6:00 (green line with diamond marker), 8:00 (blue line with square marker), and 10:00 (red line with triangle marker) on 17 March (UTC+8). Terminal points are marked every 6 hours. The starting location is set as 200 m (left panel) and 1000 m (right panel) over Hefei. The map data used in this figure are from Natural Earth.